ADVANCED ENERGY MATERIALS
www.advenergymat.de

Engineering the Site-Disorder and Lithium Distribution in the Lithium Superionic Argyrodite Li_6PS_5Br

Ajay Gautam, Marcel Sadowski, Michael Ghidiu, Nicolò Minafra, Anatoliy Senyshyn, Karsten Albe, and Wolfgang G. Zeier**

Lithium argyrodite superionic conductors, of the form Li_6PS_5X (X = Cl, Br, and I), have shown great promise as electrolytes for all-solid-state batteries because of their high ionic conductivity and processability. The ionic conductivity of these materials is highly influenced by the structural disorder of S^{2-}/X^- anions; however, it is unclear if and how this affects the Li distribution and how it relates to transport, which is critical for improving conductivities. Here it is shown that the site-disorder once thought to be inherent to given compositions can be carefully controlled in Li_6PS_5Br by tuning synthesis conditions. The site-disorder increases with temperature and can be "frozen" in. Neutron diffraction shows this phenomenon to affect the Li^+ substructure by decreasing the jump distance between so-called "cages" of clustered Li^+ ions; expansion of these cages makes a more interconnected pathway for Li^+ diffusion, thereby increasing ionic conductivity. Additionally, ab initio molecular dynamics simulations provide Li^+ diffusion coefficients and time-averaged radial distribution functions as a function of the site-disorder, corroborating the experimental results on Li^+ distribution and transport. These approaches of modulating the Li^+ substructure can be considered essential for the design and optimization of argyrodites and may be extended to other lithium superionic conductors.

1. Introduction

All-solid-state-batteries are considered as promising next-generation lithium-ion batteries that can likely deliver higher energy compared to their conventional counterparts with liquid electrolytes.[1,2] Recently, lithium thiophosphates have gained attention since they are mechanically soft for ease of processing and exhibit high ionic conductivities.[2–5] The lithium argyrodites Li_6PS_5X (X = Cl, Br, I) especially have been explored in a variety of solid-state batteries.[6–10] Whereas there are still many challenges in the context of interfacial stability, the argyrodite compositions $Li_{6+x}P_{1-x}M_xS_5I$,[6,11,12] $Li_{6+x}Sb_{1-x}M_xS_5I$ (M = Si, Ge),[13] and $Li_{6-x}PS_{5-x}(Cl, Br)_{1+x}$[3,4,14] exhibit conductivities in the range that is needed for all-solid-state-batteries. However, a better understanding of the fundamental structure–transport correlations in the argyrodites is needed to further promote even faster ionic transport.

Figure 1a shows the crystal structure of Li_6PS_5Br in the ordered structure with space group $F\bar{4}3m$;the halide ions arrange in a face-centered cubic lattice (Wyckoff position 4*a*) with PS_4^{3-} polyhedra located in the octahedral voids (P on Wyckoff 4*b* and S on Wyckoff 16*e*) and a "free" S^{2-} (not bound in polyhedra) in half of the tetrahedral sites, Wyckoff 4*d*. Li^+ forms an arrangement similar to a cage around the 4*d* site, shown in Figure 1b.[3,11,15,16] Here, the known Li^+ positions are designated T5 (Wyckoff 48*h*), T2 (Wyckoff 48*h*), and T5a (Wyckoff 24*g*) in accordance with terminology in the literature.[17–19] Previously, the jump processes were described for a T5–T5a–T5 distance (doublet jump), T5–T5 distance (intracage), and T5–T5 distance (inter-cage).[20–22] Recent studies have identified the T2 site and the T2–T2 distance (shorter intercage jump) to be crucial for the ionic transport, as it represents the shortest distance between the cages (shown in Figure 1b).[19] Besides the interesting lithium substructure, argyrodites are known to undergo anionic site-disordering; S^{2-} nominally occupies the 4*d*

A. Gautam, Dr. M. Ghidiu
Institute of Physical Chemistry
Justus-Liebig-University Giessen
Heinrich-Buff-Ring 17, D-35392 Giessen, Germany
A. Gautam, Dr. M. Ghidiu
Center for Materials Research (LaMa)
Justus-Liebig-University Giessen
Heinrich-Buff-Ring 16, D-35392 Giessen, Germany
The ORCID identification number(s) for the author(s) of this article can be found under https://doi.org/10.1002/aenm.202003369.

DOI: 10.1002/aenm.202003369

M. Sadowski, Prof. K. Albe
Institute of Materials Science
Technical University of Darmstadt
Otto-Berndt-Strasse 3, D-64287 Darmstadt, Germany
E-mail: albe@mm.tu-darmstadt.de
Dr. N. Minafra, Prof. W. G. Zeier
Institute of Inorganic and Analytical Chemistry
University of Münster
Corrensstrasse 30, 48149 Münster, Germany
E-mail: wzeier@uni-muenster.de
Dr. A. Senyshyn
Heinz Maier-Leibnitz Zentrum
Technische Universitaet München
85748 Garching, Germany

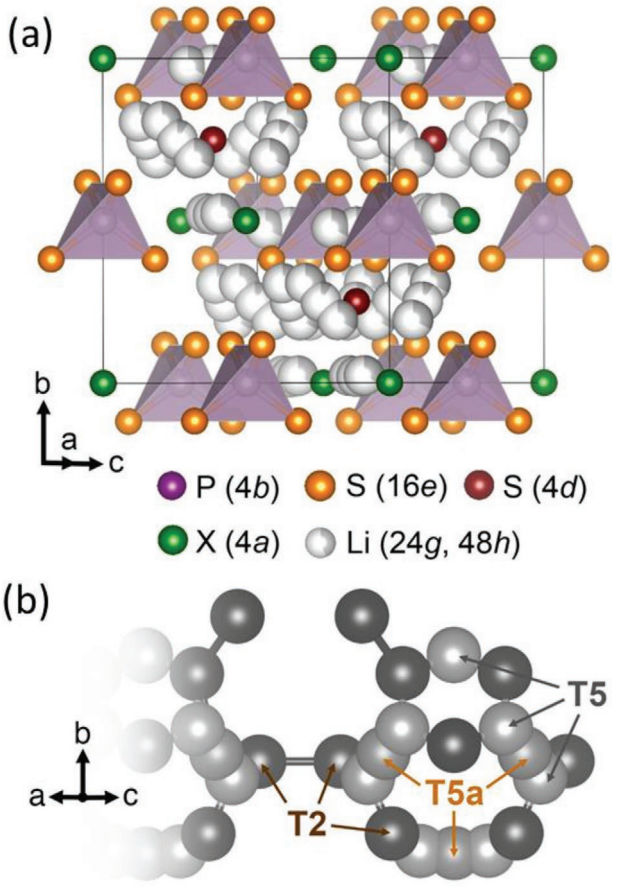

Figure 1. a) Crystal structure of Li_6PS_5Br shown in an anion ordered state with Br^- located on the Wyckoff 4*a* site and the sulfide anion (S^{2-}) on the Wyckoff 4*d* site. b) Li^+ substructure in argyrodites showing T5 (Wyckoff 48*h*), T5a (Wyckoff 24*g*), and the more recently established T2 (Wyckoff 48*h*) sites. T2 offers the shortest inter-cage jump distance (two Li cages shown connected by the T2 bridge; all atoms except Li removed for clarity).[19]

site, but it can exchange with the halide anion on 4*a* site. This site-disorder is strongest in Li_6PS_5Cl, followed by Li_6PS_5Br.[6,19] In contrast, Li_6PS_5I displays a structure without site-disorder, likely due to a more substantial ionic radius mismatch between the S^{2-} and I^-; the result is a lower ionic conductivity.[15] Substitutions for P by Si, Ge, and Sb show that the site-disorder, and subsequently ionic conductivity, in the iodide argyrodite can be increased: $Li_{6.6}P_{0.4}Ge_{0.6}S_5I$ (disorder of 6%, room temperature conductivity of 5.4 mS cm^{-1}),[6] $Li_{6.6}Sb_{0.4}Si_{0.6}S_5I$ (2%, 14.8 mS cm^{-1}),[13] and $Li_{6.7}P_{0.3}Si_{0.7}S_5I$ (12%, 2.0 mS cm^{-1}).[11] Neutron studies have shown that site-disorder leads to local charge inhomogeneity and how, in turn, this affects the different Li^+ positions, leading to more uniformly distributed Li^+ in Li_6PS_5Cl (with the higher site-disorder) compared to Li_6PS_5Br and Li_6PS_5I.[19] However, the true effect of disorder on the Li^+ substructure in all of these materials was unknown because all studies also involved changes in chemical composition that could have convoluting effects; clearly these are important interconnected aspects of these materials, but there is a lack of mechanistic studies of how the disorder alone affects Li^+ distribution.

It was only recently that site-disorder was shown to be able to be decoupled from chemical makeup by quenching techniques in the single composition Li_6PS_5Br.[23] We build upon this work here by showing synthetic methods to achieve a broad range of highly tunable site-disorders in this composition, spanning 10%–39%; in turn, neutron diffraction as well as ab initio molecular dynamics (AIMD) are used to probe and understand the details of how the Li^+ substructure is affected solely by the site-disorder. We show that higher site-disorder causes an expansion of clusters of Li^+ typically surrounding the disordered sites, leading to more interconnected diffusion pathways; this in turn is correlated to increasing ionic conductivity, up to fourfold. These findings are of fundamental importance for structure-transport correlation in these materials and may help stimulate deeper study of other materials where ion disordering is beneficial to ionic conductivity.[24]

2. Results

2.1. Structural Changes upon Quenching

The lithium substructure has been shown to be quite important for the ionic transport of the lithium argyrodites Li_6PS_5X.[3,11,13,15–19] However, usually materials with different compositions (X = Cl^-, Br^-, and I^-) are compared to each other; each has a characteristic site-disorder, but it is difficult to deconvolute which share of the conductivity differences arises from the site-disorder or from the compositional change of the halide. In order to fully understand the influence of the site-disorder on the lithium substructure, an argyrodite of a single composition in which various site-disorders can exist would be needed; our recent work[23] shows that this is indeed possible for Li_6PS_5Br when quenched from high temperature. Here we explore to what extent the site-disorder can be tailored and how it affects the lithium substructure and corresponding ionic transport.

Figure 2a shows a schematic of the synthesis approach to realize the different degrees of Br^-/S^{2-} site-disorder in Li_6PS_5Br. In order to tailor this site-disorder, Li_6PS_5Br was first synthesized from P_4S_{10}, Li_2S, and LiBr using a mechanochemical approach as reported previously.[23] Then, the obtained material was subjected to a temperature of 550 °C for 30 min, which was shown in the same work to be sufficient to achieve a fully crystalline Li_6PS_5Br.[23] The material was then slowly cooled with a rate of 4 °C h^{-1} over multiple days to ensure that this bulk batch of Li_6PS_5Br had a minimal initial disorder as a starting point for all samples. While some of this "slow-cooled" material was used for the following analysis, the rest was pressed into pellets, and again sealed into quartz ampoules, which were then inserted into a tube furnace that was already equilibrated at a specific temperature: 350, 400, 450, and 550 °C. After holding for 2 h at the desired temperature, the ampoules were quenched in liquid nitrogen to achieve rapid cooling with the hypothesis that this approach would "freeze in" the site-disorder that was achieved at the specific higher temperatures.

Rietveld refinement against neutron diffraction data was then utilized for structural characterization, especially enabling the changing Li^+ substructures to be elucidated. A representative refinement of the "slow-cooled" material can be found in Figure 2b and all neutron diffraction patterns and other refinements as well as the tabulated structural parameters can be found in Figures S1–S4 and Tables S3–S7 in the Supporting

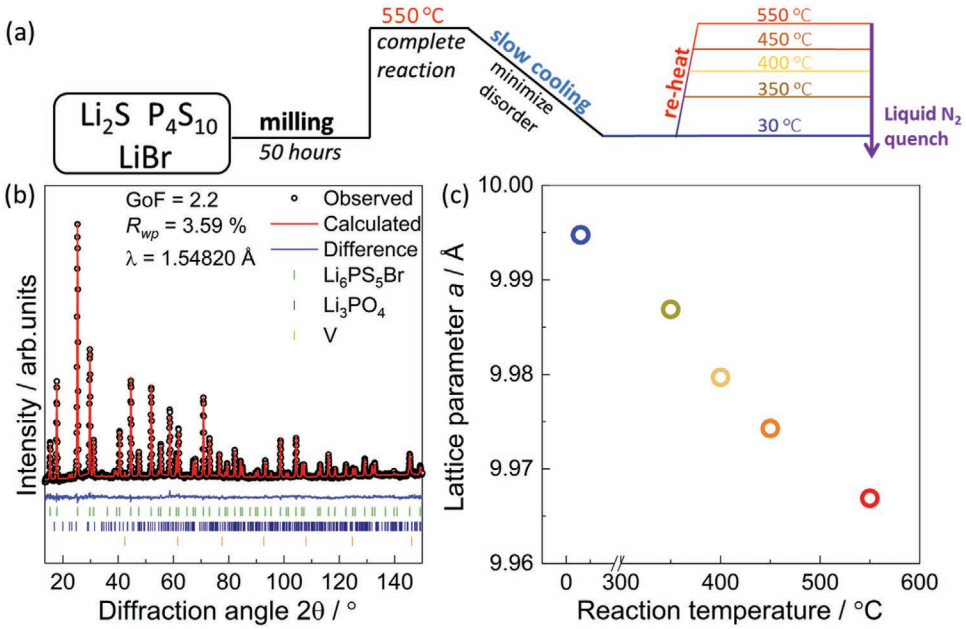

Figure 2. a) Schematic of synthesis process to control the Br^-/S^{2-} anion site-disorder in Li_6PS_5Br. b) Representative Rietveld refinement against neutron diffraction data for the slow-cooled Li_6PS_5Br. A small fraction of impurity phases corresponding to ≈0.6 wt% Li_3PO_4 are present, along with reflections from the vanadium sample container. c) The lattice parameter decreases as a function of treatment temperature. Uncertainties are smaller than the symbols. Note the axis break at 300 °C.

Information. All samples exhibit a minor impurity phase fraction of Li_3PO_4, most likely from reaction with trace amounts of H_2O during milling or handling. The amount present is small and no more than 0.6 wt% and, hence, unlikely to affect the ionic transport or the structural analysis here. With increasing treatment temperature, the lattice parameter decreases as shown in Figure 2c. This systematically decreasing lattice parameter with increasing synthesis temperature is significant and not expected. Whereas the difference in the ionic radii between the halide and the sulfide anion has been shown to affect the lattice volume in argyrodites significantly,[4,15,25–28] here no changes in composition are present that could explain this behavior. To understand this relationship, the influence of the site-disorder needs to be explored.

2.2. Energetics of Br^-/S^{2-} Site-Disorder

Similar to all lithium halide argyrodites, in Li_6PS_5Br, the Br^- anions form a face-centered cubic lattice, sitting on Wyckoff position 4*a*, which is susceptible to site-disorder.[14,15,17,26,29] Increased site-disorder involves a population of the Br^- exchanging with the S^{2-} normally sitting on 4*d* sites, around which Li^+ forms "cages" that construct the lithium substructure. From our previous work,[23] the slow-cooled sample was chosen as a minimally disordered baseline with a site-disorder of 10.0(2.4)% as determined by the Rietveld refinements. **Figure 3**b shows the different degrees of site-disorder obtained for the materials heated to various temperatures after the slow cooling process and quenching thereafter.

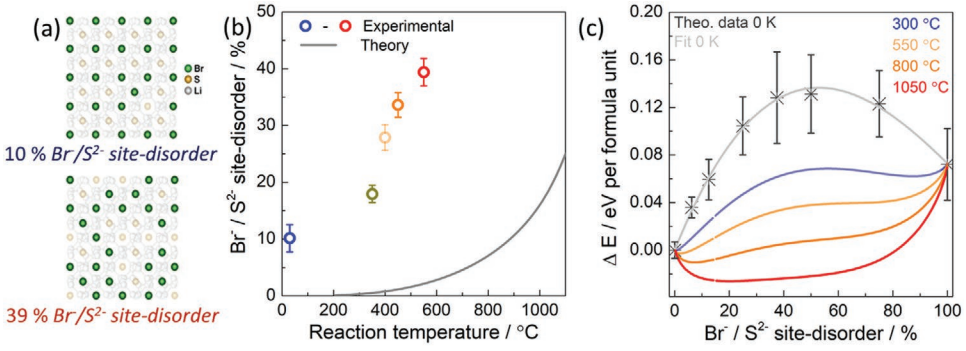

Figure 3. a) Cartoon illustrating site-disorder. b) The Br^-/S^{2-} site-disorder obtained from Rietveld refinements increases with treatment temperature. The uncertainties shown correspond to 3σ. The calculated line corresponds to predicted equilibrium site-disorder using the simulated energy difference (see 3c) while taking into account solely the configurational entropy contributions of the Br^-/S^{2-} site-disorder on the 4*a* and 4*d* sites. c) Simulated free energy difference with respect to the fully ordered structure as a function of site-disorders. Applying a fit to the data while considering the entropic contributions of the Br^-/S^{2-} site-disorder to the free energy can be calculated and is shown for different temperatures.

With increasing treatment temperature, the anionic site-disorder increases, ranging from 10.0(2.4)% to 39.0(2.1)%, clearly showing a tunability of site-disorder that has not been observed before.

In order to better understand the energetics of the Br^-/S^{2-} disordering, density functional theory (DFT) was used to calculate the total formation energy ΔE of Li_6PS_5Br with various degrees of site-disorder ranging from 0% to 100%. The site-disorder of 100% itself represents a full site inversion in which S^{2-} now occupies Wyckoff 4*a* and Br^- the 4*d* site. Figure 3c shows the energetic difference between the total energy of the disordered structures with respect to 0% site-disorder. The formation energies show that 0% is the most stable, lowest energy state and therefore thermodynamically preferred over disordered structures at 0 K. However, based on the presented quenching and slow cooling experiments it can be deduced that entropic contributions at finite temperatures lead to the stabilization of degrees of site-disorder. For one formula unit the configurational entropy ΔS_{conf} based on the Br^-/S^{2-} site-disorder w amounts to $-2k_B(w\ln(w) + (1-w)\ln(1-w))$ and allows us to calculate the free energy ΔF according to $\Delta F = \Delta E - T\Delta S_{conf}$, which is shown in Figure 3c for various temperatures. From the minimum in ΔF the equilibrium site-disorder can be determined as function of temperature and is shown in Figure 3b. Whereas the configurational entropy leads to disorder, clearly, much higher temperatures—outside of the chemical stability of Li_6PS_5Br—would be needed to arrive at the experimentally observed site-disorder. The model applied here only considers the configurational entropy due to Br^-/S^{2-} site-disorder and neglects further entropy contributions. Based on the large deviations between theory and experiment we therefore deduce that other contributions need to be taken into account in order to properly predict the degree of site-disorder as function of temperature. One potential contribution might originate from the Li^+ substructure which is correlated to the Br^-/S^{2-} site-disorder as discussed in the following section. Unfortunately, we are not aware of a model that accounts for the entropic contribution of Li^+ in superionic conductors, which would be helpful to determine the temperature-dependent stability of superionic materials.

Nevertheless, while site-disorders around 20% are typically observed in Li_6PS_5Br, here, these entropic contributions at higher temperatures, in combination with the rapid cooling that inhibits the chance for the structure to relax to a lower disorder, site-disorder can be kinetically locked in place.[23] These results show that there is an interplay between thermodynamics and kinetics that, depending on the synthesis process, affects the anionic substructure in Li_6PS_5Br; an influence on the lithium substructure is naturally expected as well.

2.3. The Lithium Substructure

Recent studies have suggested that in the argyrodite Li_6PS_5X framework, three different Li^+ positions exist, as shown in Figure 1.[18,19] These positions form cage-like substructures around the free sulfur position Wyckoff 4*d* and are designated as T5 (48*h*), T2 (48*h*), and T5a (24*g*).[18,19] Using the neutron diffraction data, the lithium positions and occupancies can be elucidated, which are further studied using AIMD simulations.

Figure S5 in the Supporting Information shows the polyhedral pathways of Li^+ diffusion in the argyrodite structure. The T5 and T2 positions form a continuous pathway of face-sharing tetrahedra in which the T2–T2 bridges connect the different Li^+ cages.[19] It has recently been suggested that the T2–T2 jump is the most important as it not only represents the shortest distance between Li^+ positions but also connects these different cages.[18,20,21] Therefore, Figure S5 in the Supporting Information shows the influence of the temperature treatment and with it the obtained site-disorder Br^-/S^{2-} as well as the lattice parameter, on the features of the lithium on T2. The additional information on the T5 polyhedral volume, T2–T5, T5–T5 distances, as well as the distances along a full path of T5–T2–T2–T5 can be found in Figure S6 in the Supporting Information. With increasing synthesis temperature and site-disorder the T2 polyhedral volume and the T2 jump area are barely affected, with a possible slight decrease, despite the changes in the lattice parameters. However, the T2–T2 distance, which facilitates the rate-determining jump between neighboring cages, decreases with increasing site-disorder from a value of 2.12(0.1) Å at 10% to 1.51(0.09) Å at 39%. These findings are substantiated by Li probability densities obtained by applying the maximum entropy method (MEM) to the diffraction data as well as the simulation data shown in Figures S7–S9 in the Supporting Information. The Li probability density allows for monitoring the change of the Li substructure on a global scale in the material. With increasing site-disorder the rather strict localization of Li occupying the T5–T5a–T5 sites starts to spread out until it forms a network with the T2 sites. Simultaneously, the T2–T2 distance between neighboring cages decreases and the T5a sites become more and more narrow.

The changes, which overall seem to be insignificant, within the occupancies of the different lithium positions can be found in Figure S10 in the Supporting Information. As a different metric, the average distance between Li^+ and the 4*d* anionic center, designated as R_{mean}, was recently proposed to help encapsulate the changes in the Li^+ occupancy and positions as well as explain transport results.[19] R_{mean} is calculated as the average distance between the three different Li^+ sites away from their central anion at Wyckoff 4*d*, weighted by the number of Li^+ ions located on the specific sites within one cage.[19] Along the series of changing site-disorders, significant deviations of R_{mean} from the 4*d* anionic center is observed (see **Figure 4**a). Increasing the site-disorder leads to a concomitant decrease in the average charge on 4*d* as the divalent sulfide is replaced by monovalent bromide. As a result, R_{mean} increases. Figure 4b shows a visual representation of R_{mean} and Figure 4c shows the Li-ion migration pathways found using the maximum entropy method for the least and most site-disordered samples, further confirming the expansion of the Li^+ cage. In order to corroborate these changes of the lithium substructure, the radial distribution function (RDF) of Li^+ around the 4*d* position was extracted from the data obtained by AIMD simulations (Figure 4d). Here, in order to test the influence of the site-disorder only, the unit cell volume was fixed during the simulations. While this approach adds some thermal strain to the calculations, it will reflect the influence of the site-disorder on the Li^+ substructure alone. First, at disorders > 50%, a shift of the Li^+ cages in the molecular dynamics simulations is visible that is then centered

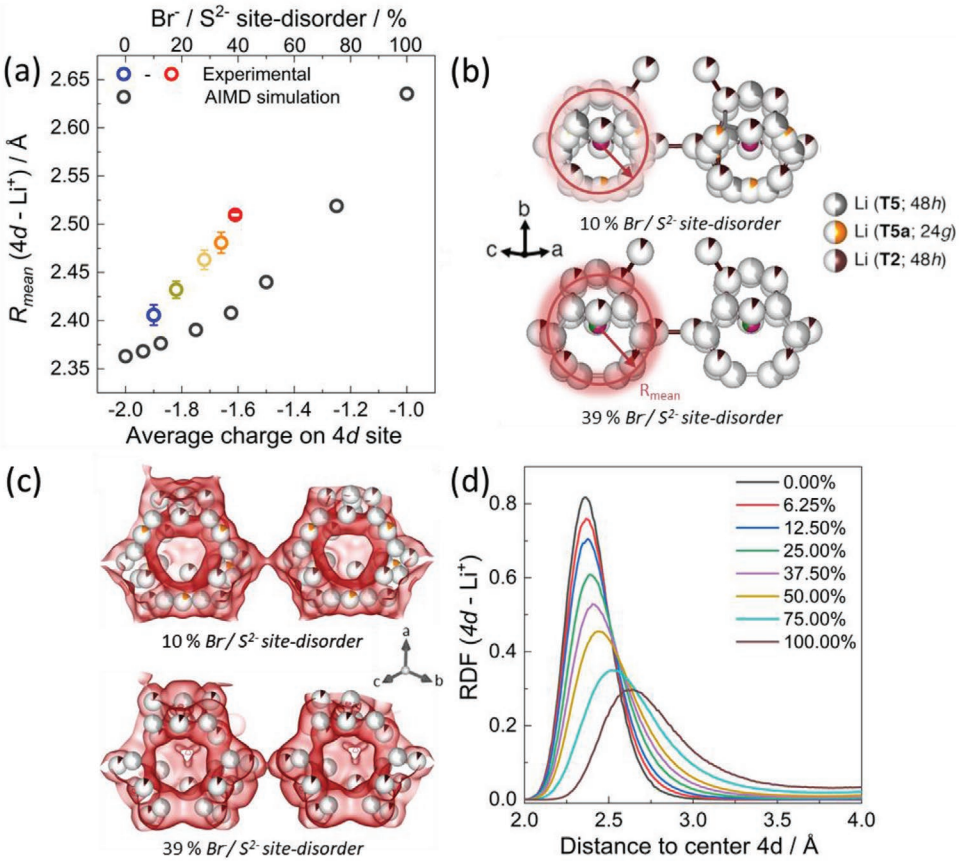

Figure 4. a) The experimental and theoretical mean distances of Li^+, R_{mean}, representing the distance between the center of the cage (Wyckoff 4*d*, free sulfide anion site), illustrated in (b). With increasing Br^-/S^{2-} site-disorder, more Br^- is located in the center position. The resulting lower anionic average charge leads to an expanding Li^+ cage and larger R_{mean}. c) The Li-ion migration pathways analyzed using the maximum entropy method (MEM). With increasing Br^-/S^{2-} site-disorder, the Li^+ cage expands and larger R_{mean} as well as shorter T2–T2 sites are found. d) Calculated radial distribution functions of Li^+ with respect to the center anion Br^-/S^{2-} on 4*d* sites, as a function of site-disorder.

around the previously nominal halide position (Wyckoff 4*a*) as shown in Figure S11 in the Supporting Information. In other words, Li^+ tends to prefer the coordination around an S^{2-} central anion, rather than the halide. In addition to the experimental R_{mean}, Figure 4a also shows the theoretical R_{mean} as a function of site-disorder. As a first approximation the theoretical R_{mean} has been determined by taking the position of the peak maximum from the first mode in the partial RDF (4*d*-Li^+). The partial RDFs (4*d*-Li^+) shown in Figure 4d clearly corroborate the experimental data: with increasing site-disorder, the Li^+ positions are shifted further outward away from the center that is occupied by the Br^-/S^{2-}. In other words, the lower charge density on 4*d* that occurs due to the tailored increasing site-disorder leads to weaker interactions between the negative charge in the center of the cage and the surrounding Li^+, which in turn then leads to shorter T2–T2 distances as shown in Figures S5 and S9 in the Supporting Information.

2.4. The Interplay of Site-Disorder and Lattice Parameter

With increasing synthesis temperature, an increasing Br^-/S^{2-} site-disorder is observed that leads to a direct expansion of the Li^+ cages centered around the Wyckoff 4*d* sites. Yet, with increasing synthesis temperature, a decreasing unit cell volume (see Figure 2) is observed. The observations of expanding lithium substructure and decreasing unit cell volume seem contradictory at first glance. It has already been shown before that the site-disorder between the 4*a* and 4*d* sites can have an impact on the lattice parameter,[14,23] but the underlying reason remained unclear.

In order to explore the reasons for the lattice parameter behavior, the simulations are compared to the experimental data. Because simulations using the applied generalized gradient approximation commonly overestimate lattice parameters, only the relative change of the lattice parameters is shown in **Figure 5**a as a function of the Br^-/S^{2-} site-disorder. Overall, in experimental data, with increasing site-disorder 10%–39%, the unit cell shrinks by around 0.28%. Whereas the experimental data only exhibit site-disorders up to 39%, the simulations are able to cover even higher degrees of site-disorder and reveal that the lattice parameters increase again once the site-disorder exceeds 50%.

To better understand the reason for the decreasing lattice volume with increasing site-disorder up to 50%, the mean distance R_{mean} of the lithium ions to the nominal halide position

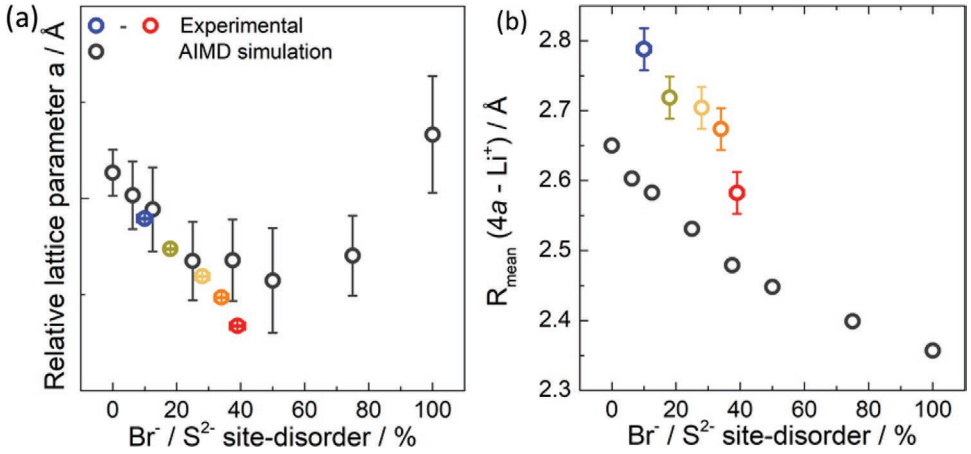

Figure 5. a) Relative change of experimental and simulated lattice parameters of Li_6PS_5Br as a function of changing site-disorders. b) The experimental and calculated mean distances R_{mean} between the Li^+ and the face-centered sublattice (Wyckoff 4*a*, halide site) as a function of site-disorder. For the simulated R_{mean}, only the position of the maximum in the RDF was used for simplicity.

Wyckoff 4*a* site is shown in Figure 5b together with the calculated partial RDF (4*a*-Li^+) in Figure S12 in the Supporting Information. While the increasing site-disorder on the 4*d* site lowers the effective negative charge inside the Li^+ cage, which drives the cages apart, the concurrently increasing occupancy of S^{2-} on the 4*a* site leads to a higher effective charge on the nominal Br^- position. With increasing site-disorder and higher negative charge on 4*a* site, R_{mean} (4*a*-Li^+) decreases and Li^+ is pulled toward the framework that forms the face-centered cubic lattice, i.e., the 4*a* positions.

For an even more detailed understanding of the connection between lattice parameters and site-disorder, the simulation data was thoroughly analyzed. We evaluated how many Li^+ ions reside in the coordination polyhedra around the central atoms on the 4*d*/4*a* sites (shown in Figure S13, Supporting Information). From Figure S13b in the Supporting Information it can be seen that the average number of Li ions around 4*d* and 4*a* at 0% site-disorder is 5.5 and 0.5, respectively. This is as expected: six Li ions form a cage centered around the S^{2-} on 4*d* site and only rarely the thermal vibrations are sufficient to shortly bring them closer to the 4*a* site. With increasing site-disorder the average number of Li around 4*d* site decreases linearly. The exact opposite happens for the average number of Li around the 4*a* site and at 100% site-disorder 0.7 and 5.3 Li reside in the coordination polyhedra around 4*d* and 4*a*, respectively. The break-even point at which on average 3.0 Li reside around the 4*a* and 4*d* sites is reached slightly above 50%. This "global" linear dependence appears trivial at first glance. However, it actually underlies more complex changes on a local scale as can be seen in Figure S13c in the Supporting Information. On a local scale the S^{2-} still attracts more Li compared to Br^-. However, at 50% site-disorder the average number of Li ions around the nominal S^{2-} (Br^-) position 4*d* (4*a*) is at a minimum (maximum). This state, therefore, corresponds to the most uniform distribution of Li and is responsible for shrinking the lattice parameter. The somewhat counter-intuitive fact that the average bond lengths between the Li ions and their respective Br^-/S^{2-} ion in the cage center (Figure S13d,e, Supporting Information) are slightly increasing plays only a minor role and does not outweigh the more uniform Li distribution. In other words, the more homogeneous charge distribution at 50% site-disorder leads to a uniform distribution of lithium ions throughout the structure, thereby shrinking the unit cell due to electrostatic reasons.

2.5. Ionic Transport Properties

The ionic transport properties of the Li_6PS_5Br series are investigated by temperature-dependent impedance spectroscopy. **Figure 6**a shows representative Nyquist plots measured at room temperature of Li_6PS_5Br with Br^-/S^{2-} site-disorder of 10%, 18%, 28%, 34%, and 39%. The impedance data were analyzed using one parallel constant phase element (CPE) and a resistor, in series with a CPE. At higher temperatures, the CPE/resistor shifted to frequencies too high to measure with the impedance analyzer, and only the tail of the blocking electrodes was used for the impedance fitting shown in Figures S15 in the Supporting Information. The geometric capacitances are around 0.8×10^{-10} to 1.8×10^{-10} F cm^{-2} and α factors of up to 0.94 can be found. These data represent a high ideality of the constant phase element and suggest that the transport is mostly dominated by the bulk contribution.[30,31] Figure 6b shows the temperature dependence of the obtained ionic conductivities, which exhibits a linear Arrhenius type behavior. The obtained room temperature conductivities and activation energy can be found in Figure 6c,d as a function of the Br^-/S^{2-} site-disorder. As recently shown, the higher disorder leads to a fourfold improvement in the ionic conductivity.[23] The conductivity of the slow-cooled samples, with the least site-disorder, exhibits a baseline of 0.5 mS cm^{-1}, which increases up to 2.0 mS cm^{-1} at 39% site-disorder. Along with the increasing conductivity, a minor increase in the activation energy is found, consistent with previously observed trends in Li_6PS_5Br.[23]

In order to assess the changing transport properties with the site-disorder, the results of the AIMD simulations are shown in **Figure 7**. The obtained mean square displacements against simulation time are shown in Figure S16 in the Supporting

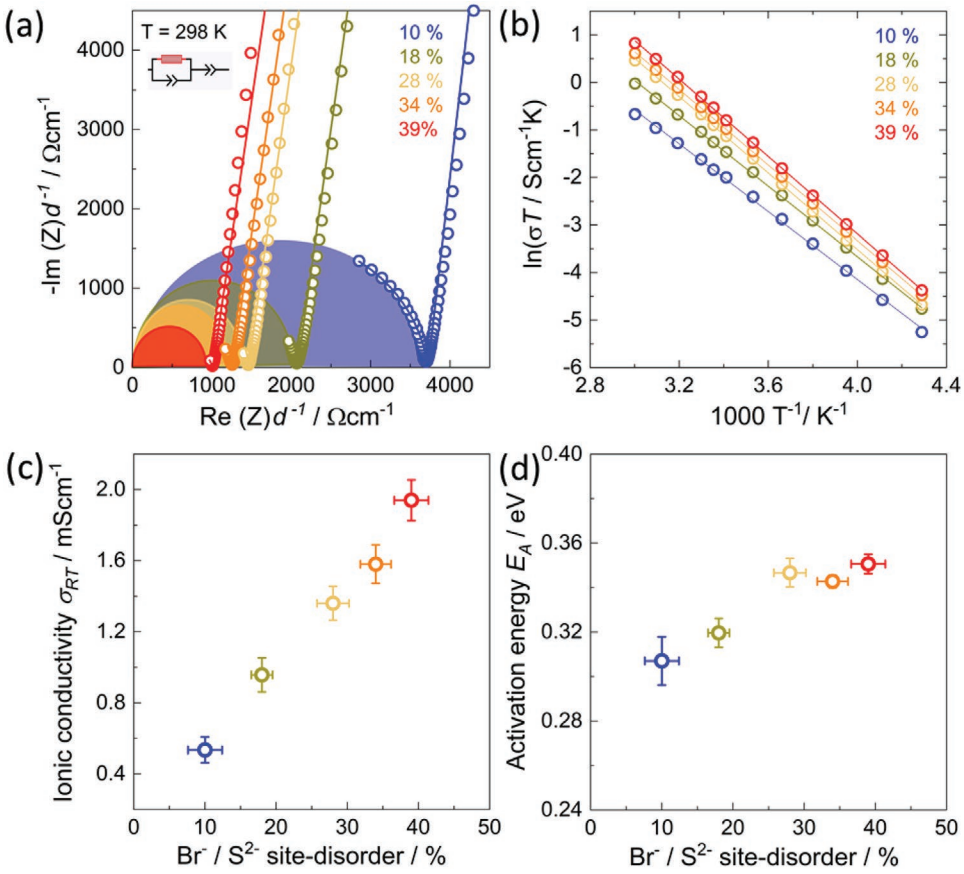

Figure 6. a) Representative fit of the impedance spectra of Li_6PS_5Br with different degrees of disorder, showing the impedance response (open circles) and the impedance fits. A bulk capacitance of ≈0.6 to 1.8 × 10^{-10} F cm^{-2} is found for the process. The impedance is shown normalized by the pellet thickness for comparison. b) Representative Arrhenius plots of the Li_6PS_5Br for different degrees of disorder. c) Room-temperature ionic conductivity and d) activation energy E_A as a function of S^{2-}/Br^- site-disorder.

Information. As often observed in the literature for argyrodites,[3,15,18,19,27] site-disorder affects the ionic transport, here shown by increasing tracer diffusion coefficients up to 50% site-disorder. As recently shown,[6,11,13] at a certain critical site-disorder the activation barriers drop significantly, corroborating that a critical degree of disorder is needed for fast transport. Furthermore, an approximately fourfold increase of the conductivity is observed when comparing between the

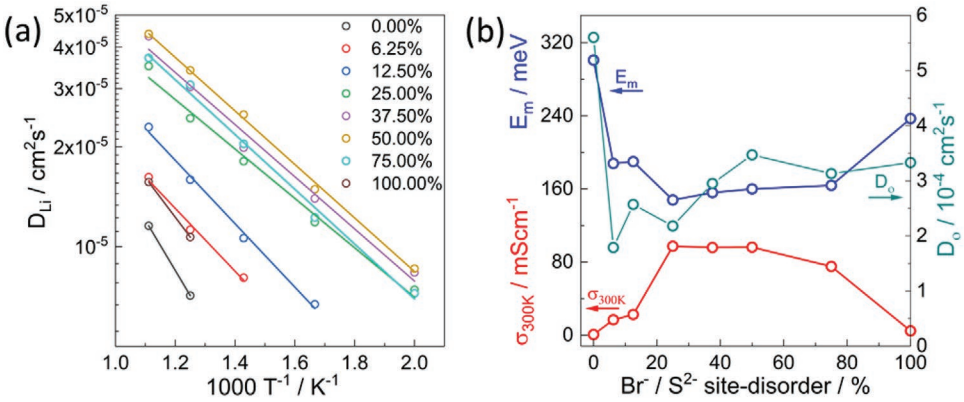

Figure 7. a) Calculated tracer diffusion coefficients as a function of temperature for changing site-disorders together with Arrhenius fits according to $D_{Li}(T) = D_0$*exp(E_m/kT). See Figure S14 in the Supporting Information for individual plots with error bars. b) Extracted fit values E_m and D_0. These fit values have been used to calculate the ionic conductivity σ_{300K} at 300 K using the Nernst–Einstein equation $\sigma(T) = D_{Li}(T)c(qZ)^2/kT$, where c is the Li number density, q is the elementary charge and for the nominal charge of the mobile species Z, a value of 1 has been used. Note that the fit for 0% and 100% site-disorder has been applied to only two data points and might therefore exhibit higher statistical uncertainties.

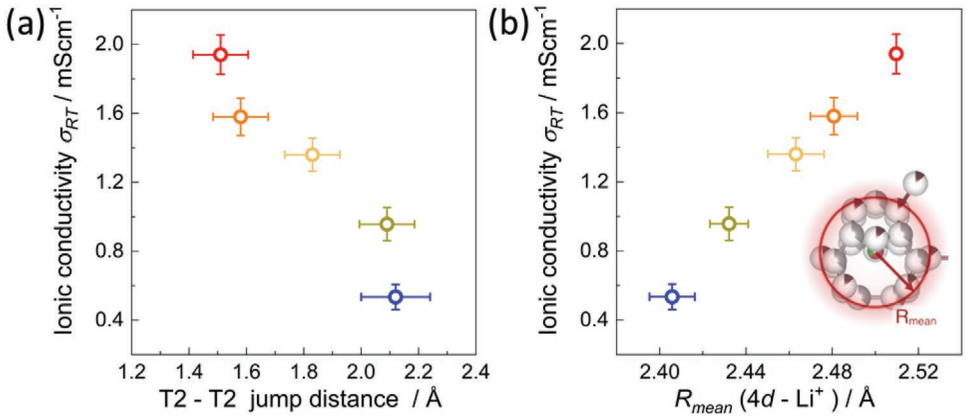

Figure 8. Room-temperature ionic conductivity as a) a function of the T2–T2 distance and b) the R_{mean} distance b) of Li^+ away from the cages, designating how far Li^+ has spread out. The shorter T2–T2 distance and longer R_{mean} due to the charge inhomogeneity leads to a fourfold increase of the ionic conductivity.

simulated structures with 12.5% and >25% site-disorder, similar to the experimental results.

3. Discussion

Changing the synthesis conditions in Li_6PS_5Br tailors the known site-disorder between Br^- and S^{2-}, which has a direct influence on the lithium substructure as well as the ionic transport. As this study has the benefit of a range of site-disorders with the same chemical composition, certain observations can be derived:

1) Considering the calculated energetics of the site-disorder, a full ordering of the anion sublattice would be preferred thermodynamically. However, at elevated temperatures, anionic site-disorder between the halide and sulfur anion seems to be prevalent. By experimental quenching, the site-disorder at the respective temperature can be kinetically frozen, which in turn makes it possible to tailor the site-disorder up to 39% and, therefore, optimize the ionic conductivity in Li_6PS_5Br.
2) Conversely, clearly the thermal history of these materials influences the structure and ionic transport. Therefore, sintering or additional heat treatments of argyrodites need to be more closely monitored and reported.
3) The disorder in the anion sublattice between S^{2-} and Br^- leads to large charge inhomogeneities as recently proposed.[19] However, the site-disorder is usually only changed by changing the halide composition; therefore the actual contribution of the different composition itself versus the amount of disorder is difficult to deconvolute. By tailoring the site-disorder between S^{2-} and Br^- experimentally in a fixed composition, strong influences on the lithium substructure are observed and can be related purely to disorder. The Li^+ positions that cluster as cages around the typical S^{2-} site move away from the center of the cage, the more Br^- occupies the S^{2-} site. The resulting decrease of the average anionic charge in the center means less strongly bound and less localized Li^+.[19] Conversely, the Li^+ is now more evenly distributed throughout the unit cell, which seems to be the reason for a decreasing lattice volume with increasing site-disorder.
4) On a global scale, the decreasing average charge on the 4*d* site (designated as the center of the Li^+ cages) and the concurrent expansion of the Li^+ cages away from the center, lead to shorter Li^+–Li^+ jumps, as represented by the shorter T2–T2 distance and longer R_{mean} (4*d*-Li^+) in **Figure8**a,b. The easier Li^+ jumps along with T2–T2 distance as well as the spatially more diffuse distribution of Li^+ are the driving factors for the observed increasing ionic conductivity and tracer diffusion coefficient in Li_6PS_5Br as a function of the tailored anionic Br^-/S^{2-} site-disorder.

4. Conclusion

In this work, we have demonstrated synthetic control over the anion site-disorder in Li_6PS_5Br. A baseline minimum site-disorder of 10% was established using a slow cooling technique[23] and higher site-disordered was tailored by subjecting Li_6PS_5Br to different temperatures followed by quenching. Even though density functional theory shows that the fully ordered structure is the most thermodynamically stable configuration, quenching is able to lock in the entropically favored site-disorder present at higher temperatures. Neutron powder diffraction and AIMD simulations show that the changing site-disorder results in differences in the local charges, which in turn directly affects the lithium distribution. A higher degree of site-disorder means more spatially distributed Li^+ and shorter Li^+–Li^+ distances responsible for the intercage jumps. The optimized site-disorder can subsequently lead to a fourfold increase of the ionic conductivity. This work provides a better understanding of how synthesis and postsynthesis conditions affect the structure, and with it the ionic transport, in lithium argyrodites. This knowledge is a stepping-stone for engineering materials properties without changing the composition of the material itself.

5. Experimental Section

Synthesis: All syntheses work was performed under an Ar atmosphere (O_2 < 1 ppm and H_2O < 2 ppm). Stoichiometric amounts of lithium

sulfide (Li_2S, Alfa-Aesar, 99.9%), phosphorus pentasulfide (P_4S_{10}, Merck, 99%), and lithium bromide (LiBr, ultradry, Alfa-Aesar, 99.99%) were mixed using an agate mortar to obtain an initial uniform mixing. For the mechanochemical synthesis, the obtained composition was placed in a 45 mL zirconia ball milling cup with 5 mm diameter milling media (40:1 mass ratio of milling media to precursor). Then the samples were ball milled (Fritsch Pulverisette 7 premium line) at 510 rpm using a ZrO_2 milling set. The milling was performed for a total of 150 cycles with intermediate cooling time (10 min rest after every 10 min of run time) to prevent excessive heating. During the process, the milling set was opened twice in the glovebox to physically remove caked powders from the wall of the cups. The obtained powder was manually pressed into a 1 cm diameter pellet and then filled into quartz ampoules. Before the filling, the quartz ampoules were carbon-coated and preheated at 800 °C under a dynamic vacuum to remove all traces of water. The quartz ampoules were sealed under vacuum.

The sealed ampoules were inserted into a tube furnace that was already equilibrated at the reaction temperature of 550° C and dwelled for 30 min, followed by cooling at a rate of 4° C h^{-1} over 5–6 d ("slow cooling"). This step served to ensure the complete formation of argyrodites and a uniform initial composition and structure.[23] Once the reaction was completed, the material was again hand-ground, pressed into pellets, and filled into quartz ampoules. The sealed ampoules were inserted into a tube furnace that was already equilibrated at specific temperatures: 350, 400, 450, and 550 °C for 2 h, followed by quenching in liquid nitrogen for rapid cooling. Each sample was synthesized three times to ensure reproducibility. The final products were hand-ground into a powder for diffraction studies and isostatically pressed into pellets for electrochemical measurements.

Neutron Powder Diffraction: High-resolution neutron powder diffraction data were collected at the Heinz Maier–Leibnitz Zentrum (research reactor FRM II, Garching b. München Germany) using the high-resolution diffractometer SPODI[15] operating with monochromatic neutrons (wavelength of $\lambda = 1.54820(2)$ Å). The strategy of data collection and experimental parameters were performed in the same way as recently shown for $Li_{6+x}P_{1-x}Ge_xS_5I$.[6,11] Approximately 2.5 g of the sample from each material was filled into a 10 mm diameter cylindrical vanadium container (wall thickness 150 µm) under argon atmosphere and then sealed using an indium wire to prevent air exposure during the measurement. Reference measurement data of an empty can were collected in high-resolution neutron powder diffraction data to flatten the background.

Rietveld Analysis: Rietveld refinements were performed using the TOPAS-Academic V6 software package.[32] The structural information obtained from the neutron powder diffraction refinement of Li_6PS_5Br from Minafra et al.[19] were used as a starting model for this study. The peak shape was described by a pseudo-Voigt function using the modified Thomson–Cox–Hasting setting. Fit indicators R_{wp}, R_{exp}, and goodness-of-fit were used to assess the quality of the refined structural model. The following parameters were initially refined: 1) scale factor, 2) ten coefficients for a Chebyshev function background, 3) peak shape, 4) lattice parameters, 5) zero error, 6) fractional atomic coordinates, 7) atomic occupancies, and finally 8) isotropic atomic displacement parameters. The stability of the refinements was ensured by allowing to refine multiple correlated parameters simultaneously. Upon refining over several cycles, the lithium thermal displacement parameter of the T5a sites resulted in unphysical negative values. Subsequently, T5a sites were removed from the structural model and, in turn, led to a too high thermal displacement parameter $B_{iso} > 9$ Å^2 for Li on the T5 sites. This high value is consistent with the literature,[15–17,19,33] in which the fast ionic exchange among the two neighboring T5 sites results in "smeared out" lithium nuclear density over the T5a positions, usually interpreted as lithium occupancy on T5a sites. Here, the unphysically high lithium thermal displacements for T5a sites can be, therefore, justified by the complex convolution of occupancy and thermal displacements of T5 and T5a sites. In order to obtain stable refinements with physically sound/looking values, the model utilized in Rietveld analysis was simplified, while keeping it consistent with other reports in literature[15,16,34] by constraining the thermal displacement values for T5a sites to be the same as T5 sites. This constraint allows obtaining positive lithium thermal displacement for both T5 and T5a sites while affecting the lithium occupancy and positions only slightly. Similar to previous studies,[15,19] at a site-disorder greater than 30%, no T5a site occupancy was found. Any attempts of refining in the 39% disorder sample give high uncertainties and near-zero occupancies values, suggesting the absence of the T5a site in the 39% site-disorder refinement. Ultimately, the reported structural models were obtained allowing to refine all these structural parameters at the same time. The obtained atomic positions, occupancies, and thermal displacements alongside with the applied constraints can be found in Tables S1–S7 in the Supporting Information.

Maximum Entropy Method Analysis: Reconstruction of nuclear densities was performed by MEM as implemented in the program Dysnomia.[35] It is based on the estimation of 3D scattering densities from a limited amount of information by restraining the maximum information entropy. The results of Rietveld refinements were used as an input and the three dimensional distribution of nuclear scattering densities was generated on a $256 \times 256 \times 256$ grid sampling the cell volume. The energetics of the lithium diffusion (activation energies) was estimated/ranked based on one-particle-potential formalism applying normalized negative nuclear densities.[36–38]

Electrochemical Impedance Spectroscopy: Total conductivity was measured using AC impedance spectroscopy. Initially, as-synthesized powders were isostatically pressed at 325 MPa for 45 min. Then, 200 nm thick gold layers were deposited on both sides of the pellet using the thermal evaporation technique and aluminum was used as a current collector for the transport measurements, following previous work.[23] All measurements were performed in pouch cell configuration and sealed under Ar atmosphere. Electrochemical impedance spectroscopy measurements were performed in the temperature range of –40–60 °C (Weiss Klimatechnik Climate Chamber) using an SP300 impedance analyzer (Biologic Science Instruments) with 10 mV amplitude with frequency ranging from 7 MHz to 100 mHz. The analyses of obtained spectra were performed using the RelaxIS 3–Impedance Spectrum Analysis software (rhd instruments, Darmstadt, Germany).

Density Functional Theory and Ab Initio Molecular Dynamics Simulations: DFT calculations have been performed using the Vienna ab initio simulation package[39–41] with the Perdew–Burke–Ernzerhof exchange-correlation functional[42,43] and projector augmented-wave pseudopotentials,[44,45] where the outermost three, five, six, and seven electrons of Li, P, S, and Br, respectively, are treated explicitly. All calculations were performed without spin polarization. For geometry optimizations of atomic structures, the cutoff energy for the plane wave basis set was set to 600 eV and a *k*-spacing of 0.25 Å^{-1} was used. The convergence thresholds for the electronic energy were 10^{-6} eV and ionic positions, cell volume and cell shape were optimized until ionic forces fell below 10^{-2} eV Å^{-1}. Furthermore, AIMD simulations were performed in the canonical ensemble with 1 fs time steps using a Nosé thermostat. Therefore, only the gamma point was sampled and the cutoff energy was set to 499 eV, which corresponds to the highest default value as specified in the pseudopotentials. For the calculations, the following workflow was applied: Initially, the structural model of Li_6PS_5Br with 0% Br^-/S^{2-} site-disorder was used as a starting structure. In order to avoid dealing with an unmanageable number of structures that can be created based on the Li sites with partial occupancies all T5a positions were only occupied with Li. This structure was geometrically optimized leading to a lattice constant of 10.2854 Å. Next, the supercell program[46] was used to generate structures with different degrees of site-disorder in a $\sqrt{2} \times \sqrt{2} \times 2$ supercell containing 16 formula units of Li_6PS_5Br. For all degrees of site-disorder (except 0% and 100%), multiple arrangements of the Br^- and S^{2-} ions among the 4*a* and 4*d* positions are possible from which only a subset can feasibly be analyzed. In the end 1 (0%), 4 (6.25%), 6 (12.5%), 6 (25%), 6 (37.5%), 10 (50%), 6 (75%), and 1 (100%) different Br^-/S^{2-} arrangements were considered for the respective degrees of site-disorder shown in brackets. These 40 structures were used as initial models to perform AIMD simulations at 500, 600, 700, 800, and 900 K. The trajectories of the AIMD runs were inspected using Ovito[47] and its python interface. This allowed to calculate Li^+ tracer

diffusion coefficients based on mean-square-displacements, to generate time-averaged RDFs and to perform further analyses. Furthermore, for each of the 40 structures, five intermediate "snapshot" structures were extracted from the AIMD at 500 K and subjected them to a full geometry optimization in order to obtain structural data and energetics based on more reasonable Li arrangements than the ones used initially.

Supporting Information

Supporting Information is available from the Wiley Online Library or from the author.

Acknowledgements

A.G. and M.S. contributed equally to this work. The research was supported by the Bundesministerium für Bildung und Forschung (BMBF) within the project FESTBATT under Grant Nos. 03XP0177A and 03XP0174A. This research used resources at the high-resolution diffractometer SPODI and monochromatic neutron source, operated by the Heinz Maier-Leibnitz Zentrum, Technische Universität München, 85748 Garching, Germany. Calculations for this research were conducted on the Lichtenberg high performance computer of the Technical University of Darmstadt. Authors thank Marvin A. Kraft for valuable discussions.

Open access funding enabled and organized by Projekt DEAL.

Conflict of Interest

The authors declare no conflict of interest.

Keywords

anionic site-disorder, diffusion, lithium substructure, solid electrolytes, solid-state batteries

Received: October 24, 2020
Revised: December 3, 2020
Published online: December 28, 2020

[1] J. Janek, W. G. Zeier, *Nat. Energy* **2016**, *1*, 16141.
[2] Y. Kato, S. Hori, T. Saito, K. Suzuki, M. Hirayama, A. Mitsui, M. Yonemura, H. Iba, R. Kanno, *Nat. Energy* **2016**, *1*, 16030.
[3] P. Adeli, J. D. Bazak, K. H. Park, I. Kochetkov, A. Huq, G. R. Goward, L. F. Nazar, *Angew. Chem.* **2019**, *58*, 8681.
[4] L. Zhou, K.-H. Park, X. Sun, F. Lalere, T. Adermann, P. Hartmann, L. F. Nazar, *ACS Energy Lett.* **2019**, *4*, 265.
[5] T. Krauskopf, S. P. Culver, W. G. Zeier, *Chem. Mater.* **2018**, *30*, 1791.
[6] M. A. Kraft, S. Ohno, T. Zinkevich, R. Koerver, S. P. Culver, A. Senyshyn, S. Indris, B. J. Morgan, W. G. Zeier, *J. Am. Chem. Soc.* **2018**, *140*, 16330.
[7] F. Walther, R. Koerver, T. Fuchs, S. Ohno, J. Sann, M. Rohnke, W. G. Zeier, J. Janek, *Chem. Mater.* **2019**, *31*, 3745.
[8] M. Chen, R. P. Rao, S. Adams, *Solid State Ionics* **2014**, *262*, 183.
[9] C. Yu, J. Hageman, S. Ganapathy, L. Van Eijck, L. Zhang, K. R. Adair, X. Sun, M. Wagemaker, *J. Mater. Chem. A* **2019**, *7*, 10412.
[10] H. Wang, C. Yu, S. Ganapathy, E. R. H. van Eck, L. van Eijck, M. Wagemaker, *J. Power Sources* **2019**, *412*, 29.
[11] S. Ohno, B. Helm, T. Fuchs, G. Dewald, M. Kraft, S. Culver, A. Senyshyn, W. Zeier, *Chem. Mater.* **2019**, *31*, 4936.
[12] F. Zhao, J. Liang, C. Yu, Q. Sun, X. Li, K. Adair, C. Wang, Y. Zhao, S. Zhang, W. Li, S. Deng, R. Li, Y. Huang, H. Huang, L. Zhang, S. Zhao, S. Lu, X. Sun, *Adv. Energy Mater.* **2020**, *10*, 1903422.
[13] L. Zhou, A. Assoud, Q. Zhang, X. Wu, L. F. Nazar, *J. Am. Chem. Soc.* **2019**, *141*, 19002.
[14] P. Wang, H. Liu, S. Patel, X. Feng, P.-H. Chien, Y. Wang, Y.-Y. Hu, *Chem. Mater.* **2020**, *32*, 3833.
[15] M. A. Kraft, S. P. Culver, M. Calderon, F. Böcher, T. Krauskopf, A. Senyshyn, C. Dietrich, A. Zevalkink, J. Janek, W. G. Zeier, *J. Am. Chem. Soc.* **2017**, *139*, 10909.
[16] N. Minafra, S. P. Culver, T. Krauskopf, A. Senyshyn, W. G. Zeier, *J. Mater. Chem. A* **2018**, *6*, 645.
[17] H. J. Deiseroth, S. T. Kong, H. Eckert, J. Vannahme, C. Reiner, T. Zaiß, M. Schlosser, *Angew. Chem., Int. Ed.* **2008**, *47*, 755.
[18] B. J. Morgan, (preprint) chemrxiv.12349703.v1.
[19] N. Minafra, M. Kraft, T. Bernges, C. Li, R. Schlem, B. J. M. W. G. Zeier, *Inorg. Chem.* **2020**, *59*, 11009.
[20] S. T. Kong, H. J. Deiseroth, C. Reiner, Ö. Gün, E. Neumann, C. Ritter, D. Zahn, *Chem. - Eur. J.* **2010**, *16*, 2198.
[21] H. J. Deiseroth, J. Maier, K. Weichert, V. Nickel, S. T. Kong, C. Reiner, *Z. Anorg. Allg. Chem.* **2011**, *637*, 1287.
[22] N. J. J. De Klerk, I. Rosłoń, M. Wagemaker, *Chem. Mater.* **2016**, *28*, 7955.
[23] A. Gautam, M. Sadowski, N. Prinz, H. Eickhoff, N. Minafra, M. Ghidiu, S. P. Culver, K. Albe, T. F. Fässler, M. Zobel, W. G. Zeier, *Chem. Mater.* **2019**, *31*, 10178.
[24] R. Schlem, S. Muy, N. Prinz, A. Banik, Y. Shao-Horn, M. Zobel, W. G. Zeier, *Adv. Energy Mater.* **2020**, *10*, 1903719.
[25] R. Schlem, M. Ghidiu, S. P. Culver, A. L. Hansen, W. G. Zeier, *ACS Appl. Energy Mater.* **2020**, *3*, 9.
[26] I. Hanghofer, M. Brinek, S. L. Eisbacher, B. Bitschnau, M. Volck, V. Hennige, I. Hanzu, D. Rettenwander, H. M. R. Wilkening, *Phys. Chem. Chem. Phys.* **2019**, *21*, 8489.
[27] I. Hanghofer, B. Gadermaier, H. M. R. Wilkening, *Chem. Mater.* **2019**, *31*, 4591.
[28] A. R. Stamminger, B. Ziebarth, M. Mrovec, T. Hammerschmidt, R. Drautz, *Chem. Mater.* **2019**, *31*, 8673.
[29] P. R. Rayavarapu, N. Sharma, V. K. Peterson, S. Adams, *J. Solid State Electrochem.* **2012**, *16*, 1807.
[30] J. T. S. Irvine, D. C. Sinclair, A. R. West, *Adv. Mater.* **1990**, *2*, 132.
[31] G. J. Brug, A. L. G. van den Eeden, M. Sluyters-Rehbach, J. H. Sluyters, *J. Electroanal. Chem.* **1984**, *176*, 275.
[32] A. A. Coelho, *TOPAS-Academic, Brisbane, Australia* **2007**.
[33] S. T. Kong, C. Reiner, H. J. Deiseroth, *Z. Anorg. Allg. Chem.* **2006**, *632*, 2100.
[34] T. Bernges, S. P. Culver, N. Minafra, R. Koerver, W. G. Zeier, *Inorg. Chem.* **2018**, *57*, 13920.
[35] K. Momma, T. Ikeda, A. A. Belik, F. Izumi, *Powder Diffr.* **2013**, *28*, 184.
[36] H. Stöffler, T. Zinkevich, M. Yavuz, A. Senyshyn, J. Kulisch, P. Hartmann, T. Adermann, S. Randau, F. H. Richter, J. Janek, S. Indris, H. Ehrenberg, *J. Phys. Chem. C* **2018**, *122*, 15954.
[37] A. Senyshyn, H. Boysen, R. Niewa, J. Banys, M. Kinka, Y. Burak, V. Adamiv, F. Izumi, I. Chumak, H. Fuess, *J. Phys. D: Appl. Phys.* **2012**, *45*, 175305.
[38] K. Momma, F. Izumi, *J. Appl. Crystallogr.* **2011**, *44*, 1272.
[39] G. Kresse, J. Hafner, *Phys. Rev. B: Condens. Matter Mater. Phys.* **1994**, *49*, 14251.
[40] G. Kresse, *J. Non-Cryst. Solids* **1995**, *192–193*, 222.
[41] G. Kresse, J. Furthmüller, *Comput. Mater. Sci.* **1996**, *6*, 15.
[42] J. P. Perdew, M. Ernzerhof, K. Burke, *Phys. Rev. Lett.* **1997**, *78*, 1396.
[43] J. P. Perdew, K. Burke, M. Ernzerhof, *Phys. Rev. Lett.* **1996**, *77*, 3865.
[44] G. Kresse, D. Joubert, *Phys. Rev. B: Condens. Matter Mater. Phys.* **1999**, *59*, 1758.
[45] P. E. Blöchl, *Phys. Rev. B: Condens. Matter Mater. Phys.* **1994**, *50*, 17953.
[46] K. Okhotnikov, T. Charpentier, S. Cadars, *J. Cheminf.* **2016**, *8*, 17.
[47] A. Stukowski, *Model. Simul. Mater. Sci. Eng.* **2010**, *18*, 015012.